ARTICLE Open Access

Fano interference of photon pairs from a metasurface

Jiho Noh[1,2], Tomás Santiago-Cruz[1,2], Chloe F. Doiron[1,2], Hyunseung Jung[1,2], Jaeyeon Yu[1,2], Sadhvikas J. Addamane[1,2], Maria V. Chekhova[3,4] and Igal Brener[1,2]✉

Abstract

Two-photon interference, a quantum phenomenon arising from the principle of indistinguishability, is a powerful tool for quantum state engineering and plays a fundamental role in various quantum technologies. These technologies demand robust and efficient sources of quantum light, as well as scalable, integrable, and multifunctional platforms. In this regard, quantum optical metasurfaces (QOMs) are emerging as promising platforms for the generation and engineering of quantum light, in particular pairs of entangled photons (biphotons) via spontaneous parametric down-conversion (SPDC). Due to the relaxation of the phase-matching condition, SPDC in QOMs allows different channels of biphoton generation, such as those supported by overlapping resonances, to occur simultaneously. In previously reported QOMs, however, SPDC was too weak to observe such effects. Here, we develop QOMs based on [110]-oriented GaAs that provide an order-of-magnitude enhancement in SPDC rate, after accounting for the spectral bandwidth, compared to any other QOMs studied to date. This boosted efficiency allows the QOMs to support the simultaneous generation of SPDC from several spectrally overlapping optical modes. Using a linear polarizer, we intentionally erase the distinguishability between the biphotons from a high-*Q* quasi-bound-state-in-the-continuum resonance and a low-*Q* Mie resonance, which results in the first-time observation of two-photon interference, shown in the form of a Fano contour, in the spectrum of biphotons. This quantum interference can enrich the generation of entangled photons in metasurfaces. Their advanced multifunctionality, improved nonlinear response, ease of fabrication, and compact footprint of [110]-GaAs QOMs position them as promising platforms to fulfill the requirements of photonic quantum technologies.

Introduction

Quantum interference is an interesting phenomenon that has facilitated many advances in quantum technologies, such as in quantum information processing[1–5], quantum networks[6], quantum imaging, sensing, and metrology[7–11]. Much of this progress is enabled by the use of entangled two-photon (biphoton) light, which can be generated by non-linear processes such as spontaneous parametric down-conversion (SPDC) or spontaneous four-wave mixing in second- and third-order non-linear materials, respectively. A quantum-mechanical effect that sparked considerable discussion in the 1990s (see, for instance, ref.[12].) is two-photon interference, a.k.a. fourth-order interference, between biphotons generated in two spatially separated non-linear materials. Specifically, when two non-linear materials are pumped coherently by the same laser beam, the biphotons emitted from the two sources may exhibit two-photon interference[13] if they are indistinguishable—even in principle[14]. This phenomenon was utilized to generate polarization-entangled photons[15–17] and is used in modern implementations of quantum non-linear interferometers[18].

In this work, we introduce a unique platform to observe two-photon interference in the spectral domain between biphotons emitted from two spatially overlapping yet distinct sources in the same non-linear medium (Fig. 1a). Our approach exploits SPDC from so-called “quantum

Correspondence: Igal Brener (ibrener@sandia.gov)
[1]Sandia National Laboratories, Albuquerque, NM 87185, USA
[2]Center for Integrated Nanotechnologies, Sandia National Laboratories, Albuquerque, NM 87185, USA
Full list of author information is available at the end of the article

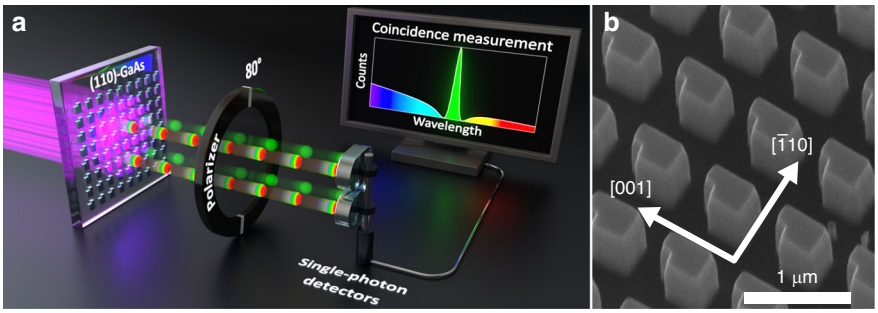

Fig. 1 Two-photon interference of biphotons in [110]-GaAs metasurfaces. a Schematic diagram of two-photon interference of biphotons emitted by spatially overlapping yet distinct resonances in [110]-GaAs metasurfaces. **b** Scanning electron microscopy (SEM) image of the metasurface at an intermediate phase of nanofabrication

optical" metasurfaces (QOMs). Metasurfaces made from non-linear materials have already revolutionized classical non-linear optics[19–23], and they have recently emerged as a promising platform for addressing the challenges of quantum state engineering. These nanostructures, carefully designed with features smaller than the wavelength of light, dramatically alter how light interacts with the material. By manipulating the phase, amplitude, and polarization of light at the nanoscale, metasurfaces enable tailored light-matter interactions far surpassing those achievable with conventional methods[19,20,22,23]. The natural extension of metasurfaces into the quantum regime, leading to QOMs, promises unprecedented control over biphoton generation, potentially overcoming the limitations inherent in bulk materials. A groundbreaking demonstration of SPDC from LiNbO3 QOMs in 2021[24] showcased the feasibility of this approach, catalyzing a series of research exploring various material systems and design strategies. Since then, researchers successfully developed SPDC sources exhibiting diverse features, including frequency multiplexing[25], spatial entanglement[26], bidirectional emission[27,28], polarization entanglement including Bell-state generation[29,30], and high-dimensional entanglement through multiphoton-state generation[31].

To observe two-photon interference, we designed metasurfaces supporting a high-quality (Q) factor resonance, namely a quasi-bound state in the continuum (qBIC), along with a low-Q in-plane Mie-like resonance, similar to our previous works[25,32]. Unlike the aforementioned works, where the in-plane Mie-like mode did not make a significant contribution to SPDC primarily due to the unfavorable crystal orientation of the metasurface's material—[001]-oriented GaAs—here, we dramatically increase the biphoton-generation rate. To this end, we fabricate the metasurfaces from a [110]-oriented GaAs wafer (Fig. 1b), whose crystal orientation simultaneously boosts the SPDC emission driven by Mie-type[30] and qBIC resonances. The transition from the conventional [001] orientation to the [110] orientation of GaAs improves the overlap integral between the electric field of interacting modes and the second-order non-linear tensor of GaAs, thereby amplifying the efficiency of SPDC and its classical reverse process, second harmonic generation (SHG). As we will show below, this strategy results in biphoton-generation rates that surpass those of any previously reported QOM by more than an order of magnitude. At the same time, the enhanced efficiency leads to the first observation of quantum interference phenomena in QOMs. This strategy pushes forward the boundaries of what is possible with QOMs without compromising their multifunctionality.

Results

Materials with zinc-blende crystalline structure, such as GaAs, AlGaAs, GaP, InGaP, etc, are particularly attractive for non-linear wave mixing because they feature some of the highest second-order susceptibilities[33], but their standard crystalline orientation—[001]—commonly used in the fabrication of resonant platforms, is not optimal for this purpose. Indeed, it has been predicted that metasurfaces fabricated on [110]- and [111]-oriented GaAs may exhibit a stronger second-order non-linear response than those fabricated on [001]-oriented GaAs[34]. This enhancement is attributed mainly to a better overlap integral between the $\chi^{(2)}$ tensor and the electric field profiles of the interacting modes. Meanwhile, some experimental studies have demonstrated the potential advantages of specific GaAs crystallographic orientations for non-linear optical processes. For instance, [110] and [111] crystallographic orientations of GaAs have been shown to facilitate normal emission of SHG and its steering in the forward or backward directions in single nanoantennas[35,36]. Motivated by these findings, R. Camacho-Morales et al. used [110]-GaAs metasurfaces to enhance the non-linear mixing of two co-propagating beams[37], while M. Yang et al. recently demonstrated strong SHG emission in the zeroth diffraction order in

monolithic [110]-GaP metasurfaces[38]. However, to the best of our knowledge, no single study has experimentally benchmarked the performance of [110] or [111] metasurfaces against their [001] counterpart in either SHG or SPDC. Moreover, the aforementioned works exploited only low-Q in-plane dipole resonances, while in this work, we use out-of-plane modes with different symmetries and much higher Q.

Our metasurface design exploits the concept of qBICs, beginning with an array of square meta-atoms that exhibit C_{4v} symmetry, supporting symmetry-protected BICs with infinite Q[39,40]. By carefully breaking this symmetry, we transform these BICs into qBICs that maintain high Q-factors while becoming experimentally accessible due to weak coupling to far-fields[41,42]. These metasurfaces support both out-of-plane electric dipole (ED) and magnetic dipole (MD) qBICs[25] (see supplementary information (SI) for a multipolar decomposition analysis). Along with qBICs, the metasurfaces also support a set of in-plane Mie-type dipole modes that stem from the initial square shape of the meta-atoms[32,41]. At resonance wavelengths, both qBICs and Mie-type modes enhance the zero-point vacuum fluctuations that seed SPDC. Due to their higher Q factors, qBICs enhance the biphoton-generation rate spectral density more significantly than low-Q in-plane Mie modes[24].

We fabricated two types of [110]-GaAs QOMs, QOM-A, and QOM-B, featuring ED-qBIC at 1588 nm and MD-qBIC at 1579 nm, respectively, to generate frequency-degenerate biphotons from our 790.8 nm continuous-wave (cw) laser, as presented in Fig. 2a, b. In addition, with the same laser, the in-plane Mie modes spanning a larger wavelength range will emit frequency-non-degenerate biphotons. The measured Q-factors of MD- and ED-qBICs were around 102, as in the previous work for SPDC with a [001]-GaAs metasurface[25]. To fabricate the QOMs, we utilized a 500 nm-thick [110]-oriented GaAs film grown by molecular beam epitaxy, off-oriented by 6° towards [111]A to improve surface quality. The details of the fabrication process, illustrated in Fig. S2, are in the "Methods" section; the metasurface dimensions are shown in Table S1.

First, we experimentally verify that SHG is enhanced in our [110]-GaAs metasurfaces. We pump the metasurfaces from the air side with a pulsed laser (350 fs, 1 MHz) in a custom-built SHG spectroscopy setup, as shown in Fig. S4a. The linear polarization of the pump laser was adjusted for each metasurface to optimize the non-linear interaction. Figure 2c shows the measured SHG efficiency $\left(P_{SH}/P_{pump}^2\right)$ as a function of wavelength for the ED-qBIC (diamonds) and MD-qBIC (circles) resonances in QOM-A and QOM-B, respectively (right dashed box). The results show that SHG peaks at the resonance wavelengths of ED-qBIC and MD-qBIC modes. Although the MD-qBIC features a higher Q-factor than that of the ED-qBIC, their SHG responses are identical. This minor discrepancy may arise from various factors, including a weaker mode overlap between the electric field of the MD-qBIC mode and the $\chi^{(2)}$ tensor, as well as a non-optimal coupling of our Gaussian pump beam to the MD-qBIC mode. In QOM-A, we can also observe SHG contributions from a low-Q in-plane Mie mode, represented by the decreasing slope between 1550 nm and 1575 nm and a Fano-type dip at 1580 nm.

For benchmarking, we further tested, under identical experimental conditions, the SHG of an ED-qBIC resonance at 1446.9 nm ($Q \sim 330$) from an [001]-GaAs metasurface (orange diamonds in Fig. 2c), which was used in our previous work for SPDC[25]. Within the effective collection numerical aperture (NA) of our setup (NA ~ 0.16), the SHG is 8-fold enhanced in both QOM-A and QOM-B compared to that of the ED-qBIC resonance in the [001]-GaAs metasurface. We, therefore, expect similar performance in SPDC. The same [001]-GaAs metasurface exhibits an MD-qBIC at 1511.8 nm with a higher Q-factor ($Q \sim 1590$), but our fs laser is spectrally too broad to efficiently excite this resonance. Notably, the response of the low-Q in-plane Mie mode in the [001]-GaAs metasurface is much weaker than in the [110]-GaAs metasurface, which is reflected in the weak and broad response indicated by green circles in Fig. 2c. To confirm the enhanced SHG efficiencies in [110]-oriented GaAs metasurfaces, we performed SHG simulations using the COMSOL Multiphysics frequency-domain finite element method solver, with the detailed methods provided in the "Methods" section. Under optimum conditions, where both the pump beam polarization and the metasurface orientation with respect to the crystalline orientations were chosen to maximize the overlap integral between the $\chi^{(2)}$ tensor and the field profiles, the simulated SHG responses of ED-qBIC (QOM-A) and MD-qBIC (QOM-B) in [110]-GaAs were 23-fold and 11-fold higher, respectively, compared to the corresponding optimum results in [001]-GaAs, when integrated over the same NA as in the experiment. These results confirm our initial hypothesis on the enhanced performance of [110]-oriented GaAs metasurfaces.

Next, we focus on the main subject of this work, which is SPDC and two-photon interference. To pump SPDC, we employ a 55 mW cw laser at $\lambda = 790.8$ nm. (See SI for optical properties of metasurfaces in this wavelength range.) We control the linear polarization of the pump beam with a half-wave plate (HWP) and focus the beam (200 μm full width at half-maximum diameter) onto the metasurface using a 60 mm focal length lens. A lens with a focal length of 18.4 mm collects the generated biphotons, which are then isolated from the pump beam through a cascade of long-pass filters with cut-on wavelengths at

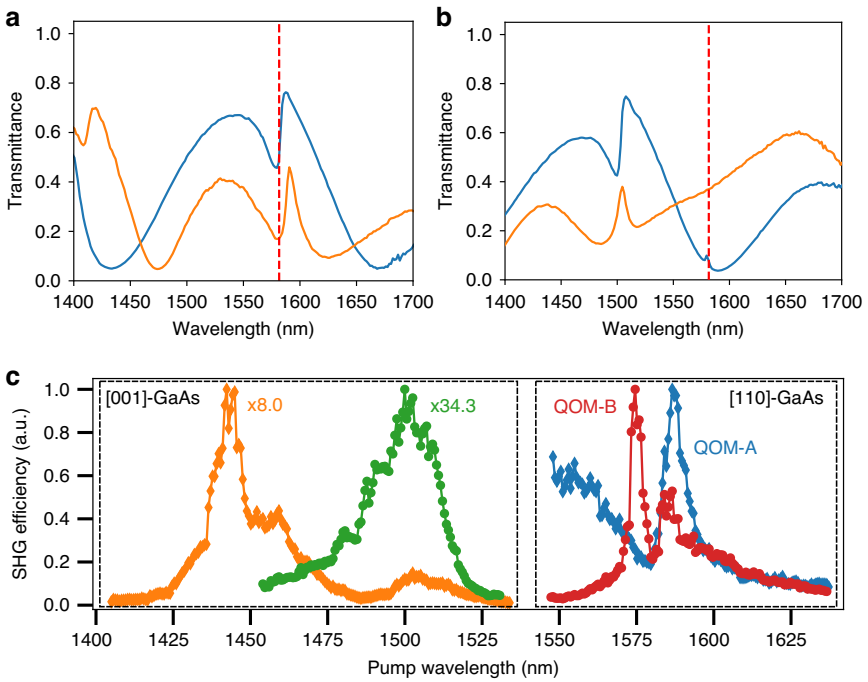

Fig. 2 White-light transmission and SHG spectroscopy of GaAs metasurfaces. a Measured white-light transmission spectra of QOM-A and **b** QOM-B for incident polarizations along the direction 45° tilted from [$\bar{1}$10] toward [001] (blue) and its orthogonal direction (orange). Red dashed line indicates double the wavelength of the pump beam. **c** SHG spectroscopy in [001]- (left dashed box) and [110]-oriented (right dashed box) GaAs metasurfaces. The diamonds and circles show the SHG efficiency from ED-qBIC and MD-qBIC resonances, respectively. At the ED-qBIC resonance, the SHG efficiency is 8-fold enhanced in [110]-GaAs metasurfaces due to an improved mode overlap. The effect of the MD-qBIC resonance in the [001]-GaAs metasurface (green circles) was not observable because the fs laser was spectrally too broad to couple to the resonance ($Q \sim 1590$)

1000 nm, 1300 nm, 1350 nm, 1400 nm, and 1450 nm. The filtered photons are then directed to a Hanbury Brown-Twiss-like setup, consisting of a 50:50 non-polarizing beam-splitter (NPBS) cube and superconducting nanowire single-photon detectors (SNSPDs). A time tagger records photodetection pulses from individual SNSPDs, and it tallies joint detection events by analyzing time intervals. This allows the measurement of the rate of simultaneous photon detections, or coincidences. For the detection using SNSPDs, we couple the photons into single-mode fibers (SMF-28) using 18.4 mm focal length lenses, resulting in an effective collection NA of ~0.14. The schematic of the experimental setup is shown in Fig. S4b.

We perform coincidence measurements by pumping the metasurfaces from the substrate side and collecting the biphotons from the air side (see Fig. 1a). Figure 3a, b show coincidence histograms acquired from QOM-A and QOM-B, respectively, for 10 min and when pumping with 5 mW. The combined timing jitter of the detectors is approximately 162 ps, and the time bin in the time tagger was set to 900 ps. The peak-to-background ratio, i.e., the second-order correlation function $g^{(2)}(0)$, exceeds two in both cases, confirming the detection of biphotons. Given that the metasurfaces were pumped above the bandgap of GaAs, incoherent photoluminescence (PL) emission accompanied SPDC, with the former being significantly more efficient than the latter. The prominent background (accidental coincidence counts) in Fig. 3a, b is attributed solely to uncorrelated coincidence events originating from PL emission.

To verify that the coincidence events observed in Fig. 3a, b stem from the resonant behavior of the metasurfaces, we examine the emission spectrum via time-of-flight spectroscopy[43]. Inserting 2 km-spools of single-mode fibers (SMF-28) on each detection arm (see experimental setup in Fig. S4b) broadened the coincidence histograms in arrival time difference. We then map the arrival time differences to photon wavelengths using calibration curves. The spectral resolution, limited by the timing jitter of the detectors, was measured to be 4.3 nm.

The spectrum measured from QOM-A (Fig. 3c) shows a distinct peak with a full width at half maximum (FWHM) of 6.4 nm at ~1580.9 nm atop a broadband pedestal. The peak originates from frequency-degenerate SPDC emission driven by the ED-qBIC resonance. This behavior is expected, as the ED-qBIC resonance wavelength closely matches twice the pump wavelength, that is, energy conservation is fulfilled when the signal and idler photons

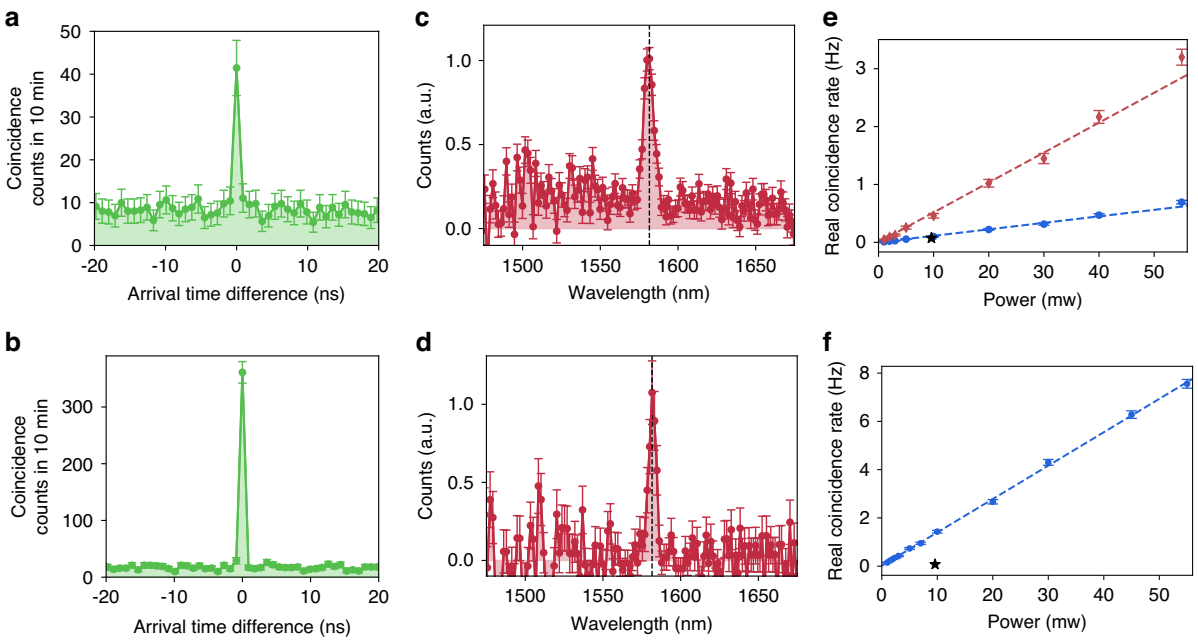

Fig. 3 Characterization of SPDC in QOM-A and QOM-B. a, **b** Coincidence histograms of SPDC from QOM-A and QOM-B, respectively. In both measurements, the pump power is 5 mW and the acquisition time is 10 min. **c**, **d** Measured SPDC spectra from QOM-A and QOM-B, respectively. Black dashed lines indicate double the wavelength of the pump laser, and their overlap with the peak in the SPDC spectra indicates that the SPDC processes are frequency-degenerate. The broad pedestal in panel **c** is due to non-degenerate SPDC driven by the in-plane Mie mode. **e**, **f** Measured power dependence of the SPDC rate from QOM-A and QOM-B, respectively. In (**e**), the red diamonds include the effect of both ED-qBIC and in-plane Mie resonances. To obtain the real coincidence rate from the ED-qBIC (blue circles), we subtracted the contribution of the in-plane Mie mode based on the data in panel **c**. Error bars indicate the statistical uncertainty. Stars in (**e**, **f**) indicate previously reported SPDC rates in [001]-GaAs metasurfaces[25]

have the same wavelength[25]. The pedestal, on the other hand, arises from frequency-non-degenerate SPDC from low-Q in-plane Mie modes in the vicinity. Remarkably, the effect of these low-Q in-plane Mie modes as the sole source for SPDC was not observed in our previous works in [001]-oriented GaAs metasurfaces[25,32], likely due to a reduced overlap integral.

The SPDC spectrum from QOM-B (Fig. 3d) shows only a clear narrow peak with a FWHM of 4.6 nm centered at ~1581.9 nm, indicating frequency-degenerate SPDC. The effect of the ED-qBIC resonance in this metasurface is not observable because of a non-optimal pump polarization and a low detection efficiency at both the resonance wavelength and its conjugate. Note that, as discussed earlier, the effect of the in-plane Mie mode is also not observed.

Then, we evaluate the performance of our QOMs by measuring the coincidence rate at various pump powers. For these measurements, we removed the fiber spools. Figure 3e, f show the real coincidence rates for QOM-A and QOM-B, respectively, calculated by subtracting the accidental coincidences from the total number of coincidences. For QOM-A, we present two data sets. The red diamonds represent the real coincidence rate that includes the contribution of both driving resonances – the ED-qBIC and the in-plane Mie mode. To isolate the SPDC efficiency due to the ED-qBIC resonance, we subtracted the contribution of the in-plane Mie-driven SPDC in each data point using the measured SPDC spectrum shown in Fig. 3d. This isolated ED-qBIC contribution is represented by the blue circles. The data show the characteristic linear dependence of the SPDC rate on the pump power, with dashed lines representing fits of the expected linear relationship. At an excitation power of 55 mW of excitation power, we observe real coincidence rates of 0.69 ± 0.03 Hz and 2.5 ± 0.1 Hz for the ED-qBIC and in-plane Mie resonances, respectively, in QOM-A, and 7.6 ± 0.2 Hz for the MD-qBIC in QOM-B. We attribute the difference in coincidence rates between the two qBICs to their distinct Q-factors and overlap integrals. While the Q-factor sets an upper bound for the conversion efficiency, a suboptimal overlap integral can further reduce this efficiency. Notably, the rate obtained from the MD-qBIC resonance is 17 times higher than that reported in a similar metasurface made of [001]-GaAs[25]. In particular, accounting for the pump power and spectral bandwidth, the rate for the MD-qBIC in QOM-B translates to 2.5×10^{-2} Hz/(mW·nm), which is an order of magnitude higher than any other SPDC rates previously reported in metasurfaces[24–26,28,30,44]. However, the rate

from the ED-qBIC alone is comparable to that of [001]-GaAs metasurface, which we attribute to the differences in *Q*-factors and pump beam diameters. In this work, the *Q*-factor of the ED-qBIC is 250, and the pump beam diameter is 200 μm, compared to 330 and 140 μm in the previous work[25]. The pump beam diameter is crucial because, although the effects may be linear with respect to pump power, the coupling efficiency is affected by the spatial mode structure. Specifically, a smaller pump area excites fewer spatial modes, thereby enhancing the collection efficiency into the single-mode fiber.

Finally, we observe two-photon interference in the spectral domain between biphotons generated by SPDC processes driven by the ED-qBIC mode and the in-plane Mie mode, respectively, in QOM-A. For the demonstration of the two-photon interference, we reinsert 2 km-spools of single-mode fibers into each detection arm for the spectral measurements, along with a HWP and a polarizing beam-splitter (PBS) placed immediately before the NPBS to serve as a polarization analyzer (see Fig. S4b).

As shown in ref.[32], biphotons from GaAs QOMs inherit the far-field polarization of the resonance modes driving the non-linear interactions. In our QOMs, the qBICs and in-plane Mie-like modes exhibit distinct far-field polarization states (see Fig. S5), and thus, biphotons emitted independently by these modes are in different polarization states. That is, even though the two SPDC processes emit biphotons within the same spectral range (i.e., spectrally indistinguishable), the biphotons are still distinguishable by their polarization states. With the polarization analyzer, we make a projection onto one polarization state and erase any possible distinguishability between the biphotons. In Fig. 4, we show the measured SPDC spectra from QOM-A with varying filtered polarization angles, with the polarization parallel to the horizontal axis denoted as 0°. As we change the angle of the analyzer, we observe the expected change in the ratio between the contributions from the qBIC and in-plane Mie resonances. When both contributions are comparable (Fig. 4c), we observe a clear Fano contour in the spectrum resulting from the two-photon interference between biphotons emitted by the two different SPDC sources. After the analyzer, the experiment cannot distinguish whether the biphotons were generated by the qBIC or by the in-plane Mie mode, and the coincidence measurement exhibits two-photon interference. (For a detailed derivation of the two-photon quantum state and the effect of the polarizer, please refer to the SI.) According to Feynman's indistinguishability criterion[14], if the biphotons cannot be distinguished—even in principle—the individual probability amplitudes should be summed, and the modulus squared should then be calculated to determine the joint detection probability. The dashed curve in Fig. 4c is a fit obtained by taking the modulus square of the sum of the amplitudes of two

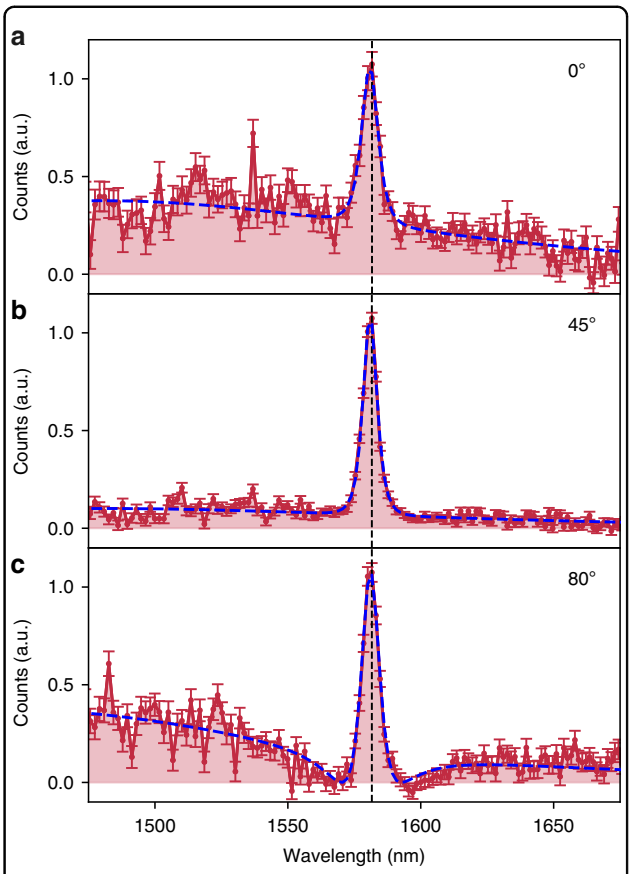

Fig. 4 Fano contours in SPDC spectra of indistinguishable biphotons. Measured SPDC spectra from QOM-A with the polarization analyzer added to the SPDC spectrum measurement setup, where the HWP was rotated to filter various polarization angles: **a** 0°, **b** 45°, and **c** 80°, with the polarization parallel to the transmission axis of the PBS denoted as 0°. The blue dashed lines show the fit to the interference of two Lorentzian-shaped resonances, while the black dashed lines indicate double the wavelength of the pump beam

Lorentzian functions, having as fitting parameters the resonance wavelengths of the qBIC and in-plane Mie modes, their linewidths, and amplitudes, see SI. The perfect agreement with the experimental data confirms Feynman's statement and the quantum nature of the interference. To our knowledge, this is the first demonstration of quantum two-photon interference enabled by biphoton emission from spatially overlapping yet distinct sources in a metasurface.

To confirm that the Fano-like spectrum arises due to the indistinguishability of the photons, we conducted additional measurements by varying the ratio of contributions between the high-*Q* qBIC and the low-*Q* in-plane Mie resonances. This was done by adjusting the polarization of the pump beam while making the biphotons distinguishable by taking out the polarization analyzer (see Fig. S6). The SPDC spectra measured in this manner clearly shows that the Fano contour, with a

distinct dip approaching zero counts, cannot be observed, thereby confirming that the Fano contour seen in Fig. 4c is indeed due to the biphoton interference.

Discussion

In summary, we have demonstrated quantum two-photon interference, a phenomenon crucial for quantum state engineering, in QOMs through biphoton emission from spatially overlapping yet distinct sources, i.e., photonic modes in [110]-GaAs metasurfaces. This interference was facilitated by the increased SPDC rates, achieved by exploiting the favorable $\chi^{(2)}$ tensor orientation of [110]-GaAs; furthermore, the quantum interference manifests as a distinctive Fano contour in the spectral analysis when the distinguishability between biphotons from high-Q qBIC and low-Q in-plane Mie resonances is erased by a polarization analyzer. Beyond the fundamental significance of observing quantum two-photon interference in metasurfaces for the first time, our work establishes [110]-GaAs metasurfaces as a powerful platform for quantum photonics, offering enhanced nonlinear response, fabrication advantages, and unprecedented multifunctionality.

While the demonstrated results are a significant step forward, challenges remain for the practical deployment of metasurface-based SPDC sources[24–30,44,45], in real-world quantum technologies. In particular, the issue of unwanted strong photoluminescence (PL)[25,27,46], accompanying SPDC emission in second-order non-linear zinc-blende materials, pumped above the bandgap, remains a key hurdle for applications such as quantum imaging with undetected photons[7], where no coincidence detection is necessary. To address these limitations, we suggest further exploration of second-order non-linear zinc-materials materials with higher energy bandgaps, such as AlGaAs, which offer greater transparency in the red wavelength range while preserving comparable second-order nonlinearity. Moreover, materials with even higher energy bandgaps, such as InGaP[30] or GaP, offer potential solutions, with GaP being particularly useful for mid-infrared applications[8,9] such as microscopy with undetected photons.

Materials and methods

Metasurface fabrication

To fabricate the QOMs, we utilized a 500 nm-thick [110]-oriented GaAs film grown by molecular beam epitaxy. The GaAs wafer was grown off-orientated by 6° towards [111]A to improve surface quality. The metasurfaces consist of square arrays of broken-symmetry meta-atoms (Fig. 1), with detailed dimensions provided in the SI. The fabrication process, illustrated in Fig. S2, involved several steps to ensure optimal performance. We began with electron-beam lithography (JEOL, JBX-6300FS) using a negative-tone resist, 6% hydrogen silsesquioxane (HSQ) solution in MIBK. To address adhesion issues caused by the inherent roughness of the [110]-GaAs surface, we deposited a 7 nm SiN layer by plasma-enhanced chemical vapor deposition (PECVD) before applying the HSQ. After patterning and development (25% TMAH, 85 °C, for 30 s), we removed the SiN layer and etched the GaAs using reactive ion etching (RIE) with a gas mixture of BCl3, Cl2, Ar, and N2 (10:10:10:1.5 sccm). The sample was then flip-chip bonded to a sapphire substrate using epoxy (353ND, EPO-TEK), followed by GaAs substrate removal through mechanical lapping and wet-etching with citric acid and phosphoric acid solutions.

Nonlinear SHG simulations

Employing the standard undepleted pump approximation, we followed a two-step process for the simulation: First, we simulated the linear response of the metasurface at the fundamental wavelength, where the pump beam was incident from the air side. The resulting local field distributions were then used to compute the induced bulk second-order polarization inside the meta-atom. Second, this bulk second-order polarization served as the sole source term for the electromagnetic simulation at the harmonic wavelength, generating the SH field, and we computed the far-field SHG intensity within the effective collection NA. Surface non-linear effects[47] were not considered in this simulation. Under optimum conditions, where the pump beam polarization and the metasurface orientation with respect to the crystalline directions were chosen to maximize the overlap integral between the $\chi^{(2)}$ tensor and the field profiles, the simulated SHG nonlinear conversion factors of QOM-A (ED-qBIC) and QOM-B (MD-qBIC) in [110]-GaAs was 23- and 11-fold higher, respectively, than the corresponding optimum results in [001]-GaAs.

Acknowledgements

This work was supported by the U.S. Department of Energy (DOE), Office of Basic Energy Sciences, Division of Materials Sciences and Engineering and performed, in part, at the Center for Integrated Nanotechnologies, an Office of Science User Facility operated for the U.S. DOE Office of Science. Sandia National Laboratories is a multi-mission laboratory managed and operated by National Technology and Engineering Solutions of Sandia, LLC., a wholly owned subsidiary of Honeywell International, Inc., for the U.S. DOE's National Nuclear Security Administration under contract DE-NA0003525. This paper describes objective technical results and analysis. Any subjective views or opinions that might be expressed in the paper do not necessarily represent the views of the U.S. DOE or the United States Government. M.V.C. is part of the Max Planck School of Photonics, supported by BMBF, Max Planck Society and Fraunhofer Society and was funded by the Deutsche Forschungsgemeinschaft (DFG, German Research Foundation), Project 311185701.

Author details

[1]Sandia National Laboratories, Albuquerque, NM 87185, USA. [2]Center for Integrated Nanotechnologies, Sandia National Laboratories, Albuquerque, NM 87185, USA. [3]Max Planck Institute for the Science of Light, 91058 Erlangen,

Germany. [4]Friedrich-Alexander-Universität Erlangen-Nürnberg, 91058 Erlangen, Germany

Author contributions

J.N., T.S., M.C., and I.B. conceived the project. J.N. performed numerical simulations and designed, fabricated, and characterized the sample. J.N. and T.S. performed SPDC experiments and data analysis. J.N., C.D., and H.J. developed the fabrication process. J.N., T.S., and J.Y. performed SHG experiments. S.A. grew the [110]GaAs wafer. I.B. and M.C. supervised all aspects of the project. All authors contributed to writing the manuscript.

Data availability

The data that support the findings of this study are available from the corresponding author on reasonable request.

Conflict of interest

The authors declare no competing interests.

Supplementary information The online version contains supplementary material available at https://doi.org/10.1038/s41377-025-01998-5.

Received: 6 March 2025 Revised: 11 July 2025 Accepted: 31 July 2025
Published online: 17 October 2025

References

1. Stobińska, M. et al. Quantum interference enables constant-time quantum information processing. *Sci. Adv.* **5**, eaau9674 (2019).
2. Qiang, X. G. et al. Large-scale silicon quantum photonics implementing arbitrary two-qubit processing. *Nat. Photonics* **12**, 534–539 (2018).
3. Knill, E., Laflamme, R. & Milburn, G. J. A scheme for efficient quantum computation with linear optics. *Nature* **409**, 46–52 (2001).
4. Spring, J. B. et al. Boson sampling on a photonic chip. *Science* **339**, 798–801 (2013).
5. Tillmann, M. et al. Experimental boson sampling. *Nat. Photonics* **7**, 540–544 (2013).
6. Bao, J. M. et al. Very-large-scale integrated quantum graph photonics. *Nat. Photonics* **17**, 573–581 (2023).
7. Lemos, G. B. et al. Quantum imaging with undetected photons. *Nature* **512**, 409–412 (2014).
8. Paterova, A. V. et al. Hyperspectral infrared microscopy with visible light. *Sci. Adv.* **6**, eabd0460 (2020).
9. Kviatkovsky, I. et al. Microscopy with undetected photons in the mid-infrared. *Sci. Adv.* **6**, eabd0264 (2020).
10. Clark, A. S. et al. Special topic: quantum sensing with correlated light sources. *Appl. Phys. Lett.* **118**, 060401 (2021).
11. Defienne, H. et al. Advances in quantum imaging. *Nat. Photonics* **18**, 1024–1036 (2024).
12. Mandel, L. Quantum effects in one-photon and two-photon interference. *Rev. Mod. Phys.* **71**, S274–S282 (1999).
13. Burlakov, A. V. et al. Interference effects in spontaneous two-photon parametric scattering from two macroscopic regions. *Phys. Rev. A* **56**, 3214–3225 (1997).
14. Feynman, R. P., Leighton, R. B. & Sands, M. *The Feynman Lectures on Physics: Volume 3: Quantum Mechanics* (Addison-Wesley, 1965).
15. Kwiat, P. G. et al. Ultrabright source of polarization-entangled photons. *Phys. Rev. A* **60**, R773–R776 (1999).
16. Burlakov, A. V. et al. Collinear two-photon state with spectral properties of type-I and polarization properties of type-II spontaneous parametric down-conversion: preparation and testing. *Phys. Rev. A* **64**, 041803 (2001).
17. Brida, G. et al. Dispersion spreading of biphotons in optical fibers and two-photon interference. *Phys. Rev. Lett.* **96**, 143601 (2006).
18. Chekhova, M. V. & Ou, Z. Y. Nonlinear interferometers in quantum optics. *Adv. Opt. Photonics* **8**, 104–155 (2016).
19. Chen, H. T., Taylor, A. J. & Yu, N. F. A review of metasurfaces: physics and applications. *Rep. Prog. Phys.* **79**, 076401 (2016).
20. Li, G. X., Zhang, S. & Zentgraf, T. Nonlinear photonic metasurfaces. *Nat. Rev. Mater.* **2**, 17010 (2017).
21. Krasnok, A., Tymchenko, M. & Alù, A. Nonlinear metasurfaces: a paradigm shift in nonlinear optics. *Mater. Today* **21**, 8–21 (2018).
22. Sain, B., Meier, C. & Zentgraf, T. Nonlinear optics in all-dielectric nanoantennas and metasurfaces: a review. *Adv. Photonics* **1**, 024002 (2019).
23. Vabishchevich, P. & Kivshar, Y. Nonlinear photonics with metasurfaces. *Photonics Res.* **11**, B50–B64 (2023).
24. Santiago-Cruz, T. et al. Photon pairs from resonant metasurfaces. *Nano Lett.* **21**, 4423–4429 (2021).
25. Santiago-Cruz, T. et al. Resonant metasurfaces for generating complex quantum states. *Science* **377**, 991–995 (2022).
26. Zhang, J. H. et al. Spatially entangled photon pairs from lithium niobate nonlocal metasurfaces. *Sci. Adv.* **8**, eabq4240 (2022).
27. Son, C. et al. Photon pairs bi-directionally emitted from a resonant metasurface. *Nanoscale* **15**, 2567–2572 (2023).
28. Weissflog, M. A. et al. Directionally tunable co- and counterpropagating photon pairs from a nonlinear metasurface. *Nanophotonics* **13**, 3563–3573 (2024).
29. Jia, W. H. et al. Polarization-entangled Bell state generation from an epsilon-near-zero metasurface. *Sci. Adv.* **11**, eads3576 (2025).
30. Ma, J. Y. et al. Nonlinearity symmetry breaking for generating tunable quantum entanglement in semiconductor metasurfaces. *Sci. Adv.* **11**, eadu4133 (2025).
31. Li, L. et al. Metalens-array–based high-dimensional and multiphoton quantum source. *Science* **368**, 1487–1490 (2020).
32. Noh, J. et al. Quantum pair generation in nonlinear metasurfaces with mixed and pure photon polarizations. *Nano Lett.* **24**, 15356–15362 (2024).
33. Shoji, I. et al. Absolute scale of second-order nonlinear-optical coefficients. *J. Optical Soc. Am. B* **14**, 2268–2294 (1997).
34. Liu, S. et al. An all-dielectric metasurface as a broadband optical frequency mixer. *Nat. Commun.* **9**, 2507 (2018).
35. Sautter, J. D. et al. Tailoring second-harmonic emission from (111)-GaAs nanoantennas. *Nano Lett.* **19**, 3905–3911 (2019).
36. Xu, L. et al. Forward and backward switching of nonlinear unidirectional emission from GaAs nanoantennas. *ACS Nano* **14**, 1379–1389 (2020).
37. Camacho-Morales, R. et al. Infrared upconversion imaging in nonlinear metasurfaces. *Adv. Photonics* **3**, 036002 (2021).
38. Yang, M. Y. et al. Second harmonic generation in monolithic gallium phosphide metasurfaces. *Nanophotonics* **13**, 3311–3319 (2024).
39. Hsu, C. W. et al. Bound states in the continuum. *Nat. Rev. Mater.* **1**, 16048 (2016).
40. Koshelev, K. et al. Asymmetric metasurfaces with high-*Q* resonances governed by bound states in the continuum. *Phys. Rev. Lett.* **121**, 193903 (2018).
41. Campione, S. et al. Broken symmetry dielectric resonators for high quality factor Fano metasurfaces. *ACS Photonics* **3**, 2362–2367 (2016).
42. Vabishchevich, P. P. et al. Enhanced second-harmonic generation using broken symmetry III–V semiconductor Fano metasurfaces. *ACS Photonics* **5**, 1685–1690 (2018).
43. Valencia, A. et al. Entangled two-photon wave packet in a dispersive medium. *Phys. Rev. Lett.* **88**, 183601 (2002).
44. Ma, J. Y. et al. Polarization engineering of entangled photons from a lithium niobate nonlinear metasurface. *Nano Lett.* **23**, 8091–8098 (2023).
45. Ma, J. Y. et al. Quantum imaging using spatially entangled photon pairs from a nonlinear metasurface. *eLight* **5**, 2 (2025).
46. Santiago-Cruz, T. et al. Entangled photons from subwavelength nonlinear films. *Opt. Lett.* **46**, 653–656 (2021).
47. Gennaro, S. D. et al. Cascaded optical nonlinearities in dielectric metasurfaces. *ACS Photonics* **9**, 1026–1032 (2022).